

Quantitative Analysis of Calcium Phosphate Nanocluster Growth Using Time-of-Flight Medium-Energy-Ion-Scattering Spectroscopy

Jimin Park,^{†,‡,⊥} Ki Dong Yang,^{†,⊥} Na-Young Kim,[§] Kang-Won Jung,^{||} Viet-Duc Le,[§] Hee-Jin Lim,^{||} Junghyun An,[†] Kyoungsuk Jin,[†] Yong-Hyun Kim,^{§,⊥} Ki Tae Nam,^{*,†,⊥} and DaeWon Moon^{*,||}

[†]Department of Materials Science and Engineering, Seoul National University, Seoul 151-744, Republic of Korea

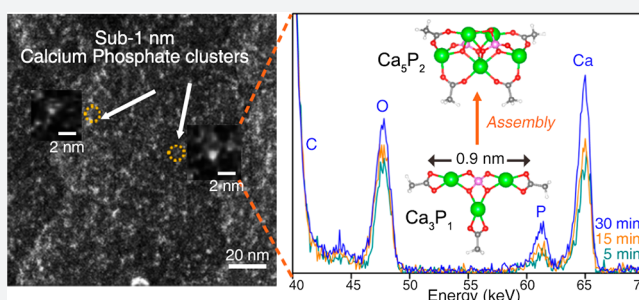
[‡]Center for Biomaterials, Korea Institute of Science & Technology, S, 14 Hwarang-ro, Seongbuk-gu, Seoul 02792, Republic of Korea

[§]Graduate School of Nanoscience and Technology, Korea Advanced Institute of Science and Technology (KAIST), Daejeon 305-701, Republic of Korea

^{||}Department of New Biology, DGIST, Dalseong, Daegu 711-873, Republic of Korea

S Supporting Information

ABSTRACT: One of the remaining challenges in material chemistry is to unveil the quantitative compositional/structural information and thermodynamic nature of inorganic materials especially in the initial nucleation and growth step. In this report, we adopted newly developed time-of-flight medium-energy-ion-scattering (TOF-MEIS) spectroscopy to address this challenge and explored heterogeneously grown nanometer-sized calcium phosphate as a model system. With TOF-MEIS, we discovered the existence of calcium-rich nanoclusters ($\text{Ca}/\text{P} \sim 3$) in the presence of the non-collagenous-protein-mimicking passivating ligands. Over the reaction, these clusters progressively changed their compositional ratio toward that of a bulk phase ($\text{Ca}/\text{P} \sim 1.67$) with a concurrent increase in their size to ~ 2 nm. First-principles studies suggested that the calcium-rich nanoclusters can be stabilized through specific interactions between the ligands and clusters, emphasizing the important role of template on guiding the chemical and thermodynamic nature of inorganic materials at the nanoscale.



INTRODUCTION

Despite recent advances in the field of nanomaterials, illustrating their exact nucleation and growth mechanism at the ultrasmall scale has remained difficult to achieve.^{1–3} By completing the whole nucleation and growth scheme, we can develop new methods that enable precise and high-throughput nanomaterial design.^{4–8} Moreover, it can also be applied to understand fundamental biological phenomena, such as biomineralization or pathological situations.^{9–12}

The emergence of time-of-flight medium-energy-ion-scattering (TOF-MEIS) spectroscopy presents new opportunities for exploring nucleation and the growth mechanism of inorganic materials via quantitative depth profiling with single-atomic-layer resolution.¹³ Compared to conventional MEIS based on a toroidal electrostatic energy analyzer with angular and energy dispersion that has been used to investigate elemental and structural depth profiles in nanomaterials, the collection efficiency of TOF-MEIS is significantly improved by more than 3 orders by using a large delay line detector with 120 mm diameter eliminating angular and energy dispersion, which minimizes possible ion-beam damage and eliminates the ion-neutralization problem.¹⁴ Recently, we proved that TOF-MEIS could acquire quantitative compositional and structural data from nanometer-scale particles that cannot be achieved by

energy-dispersive X-ray spectroscopy (EDS) or X-ray photoelectron spectroscopy (XPS) techniques with a depth resolution of more than 1–2 nm.¹³ Moreover, in contrast to transmission electron microscopy (TEM), which characterizes each nanocluster, TOF-MEIS obtains the representative average information from billions of nanoclusters on the relatively large detection area ($500 \times 750 \mu\text{m}^2$).^{13–15}

On the basis of these advantages of TOF-MEIS, we investigated its potential for revealing nucleation and growth of inorganic materials at the nanoscale. We selected heterogeneously grown calcium phosphate as a model system, as it is one of the most important inorganic materials in biological processes.^{16–21} In particular, the discovery of the formation route of the calcium phosphate compound is highly important in understanding the bone mineralization mechanism and pathological situations, such as arteriosclerosis.^{22–26} Conventionally, it was thought that nucleation proceeds via the attachment of basic monomers, and the nuclei smaller than a critical size dissolve into monomers.² However, the recent discovery of nanometer-sized species whose sizes are considerably smaller than the critical size is challenging this

Received: July 6, 2018

Published: August 30, 2018

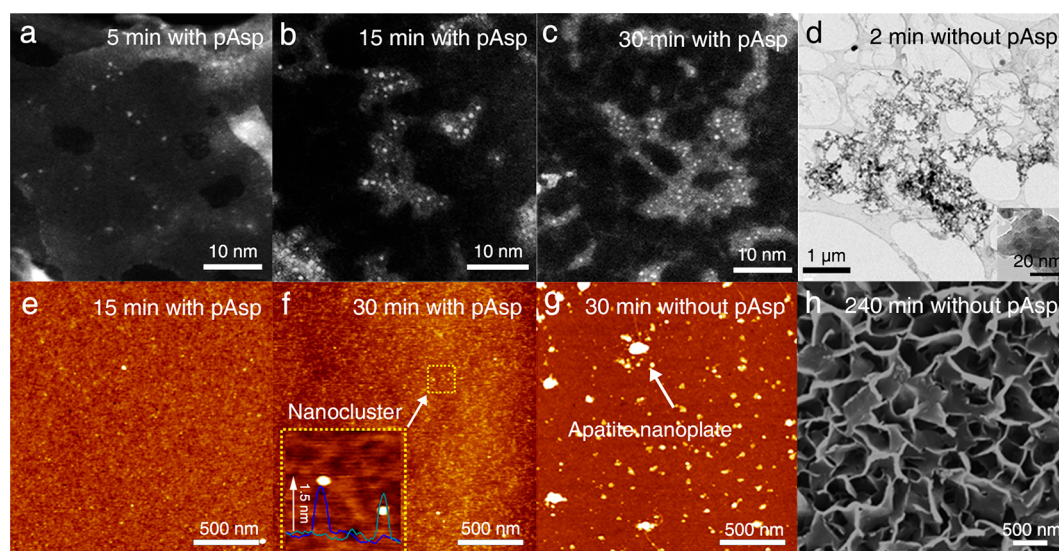


Figure 1. Observation of nanometer-scale calcium phosphate clusters in the presence of nucleation inhibitor, polyaspartic acid (pAsp). Cs-corrected STEM images of calcium phosphate clusters formed in the presence of pAsp, over time: (a) 5, (b) 15, and (c) 30 min of reaction. Approximately 1–2 nm amorphous calcium phosphate clusters were clearly observed as white dots, and their coverage increased as the reaction proceeded. (d) In the absence of pAsp, even after 2 min of the reaction, calcium phosphate aggregates were found, composing 10–20 nm amorphous calcium phosphate compounds (inset). AFM images of nanometer-scale clusters formed in the presence of pAsp over time: (e) 15 and (f) 30 min. Enlarged AFM image of the selected area of part f for showing the height of the nanoclusters (inset). (g) AFM and (h) SEM images of calcium phosphate compounds formed in the absence of pAsp. Even after 30 min of the reaction, 20 ~30 nm thick apatite plates were already found.

long-lived belief;^{27,28} there have been intense debates on whether the existence of these species can be explained by classical pictures of nucleation theory.^{29–33} Because of their extremely small size and very short lifetime,^{27,28} the exact chemical and thermodynamic information that can provide insight into the above questions remains elusive.

In the case of calcium phosphate, it has been commonly believed that nucleation proceeds by involvement of the nanometer-scale species combined with collagen and non-collagenous proteins, such as osteocalcin.^{16–21} Whereas early investigations proposed that these species include $\text{Ca}_9(\text{PO}_4)_6$ clusters,²⁵ a recent study found unstable, 1 nm calcium triphosphate complexes during homogeneous nucleation.²⁹ Similar attempts to understand the initial nucleation have been made for the calcium carbonate case, and it was revealed that factors that affect classical nucleation rate, such as Ca ion binding and interfacial free energy, play a pivotal role in the nucleation.^{34,35} These pioneering breakthroughs in calcium carbonate research can be applied to calcium phosphate studies, and new approaches considering the roles of those factors on initial nucleation can provide unprecedented opportunities for bridging the gap among current disparate views and further understanding of a more general nucleation process in nature.

In addition to the introduction of a new analytical tool, we developed a strategy that mimics the templated nucleation and growth process of calcium phosphate *in vivo*. Inspired by noncollagenous proteins inhibiting *in vivo* calcium phosphate nucleation,^{16,18} we utilized water-soluble carboxyl-rich ligands (polyaspartic acid; pAsp) to stabilize the nanometer-sized calcium phosphate and slow down their initial nucleation and growth kinetics. The stabilized species underwent slow heterogeneous nucleation onto a collagen-mimicking carboxyl-terminated self-assembled monolayer (SAM) in a controlled manner.

Taken together, we could track the quantitative information on template-guided-grown nanometer-sized calcium phosphate with TOF-MEIS analyses. One of the interesting observations in our study is that approximately 1 nm species comprising three calcium ions and one phosphate ion exist in the initial nucleation. Theoretical calculations showed that these calcium-rich clusters can stably exist through the passivation of the carboxyl-rich ligands. By combining the cutting-edge experimental tools with theoretical considerations, we found that passivating ligands can directly determine the stoichiometry and the stability of the calcium phosphate nanoclusters in a heterogeneous system.

RESULTS AND DISCUSSION

Figure 1a–c shows representative spherical-aberration-corrected scanning transmission electron microscopy (Cs-corrected STEM) images of nanometer-sized calcium phosphate clusters in our system. After 5 min of the reaction in the presence of pAsp, approximately 1–2 nm calcium phosphate clusters were observed with a very low coverage. Point EDS spectra of these clusters exhibited Ca and P peaks (Supporting Information, Figure S1). Unfortunately, the exact Ca-to-P molar ratio could not be calculated because of low Ca and P peak intensity. The coverage of these clusters increased over time; after 30 min of the reaction, polymeric-shaped aggregates consisting of these clusters were detected (Figure 1a–c), which is also confirmed by atomic force microscopy (AFM) (Figure 1e,f). Additionally, helium ion microscopy (HIM) images clearly presented the existence of the nanoclusters and their growth onto SAM-treated diamond-like-carbon (DLC) substrates (Figure 2a–d). After 15 min of the reaction, approximately 1–2 nm nanoclusters were positioned onto the substrates, and their size and coverage increased gradually during the reaction (Figure 2b–d). At the end of the reaction, after 240 min, similar polymeric aggregates

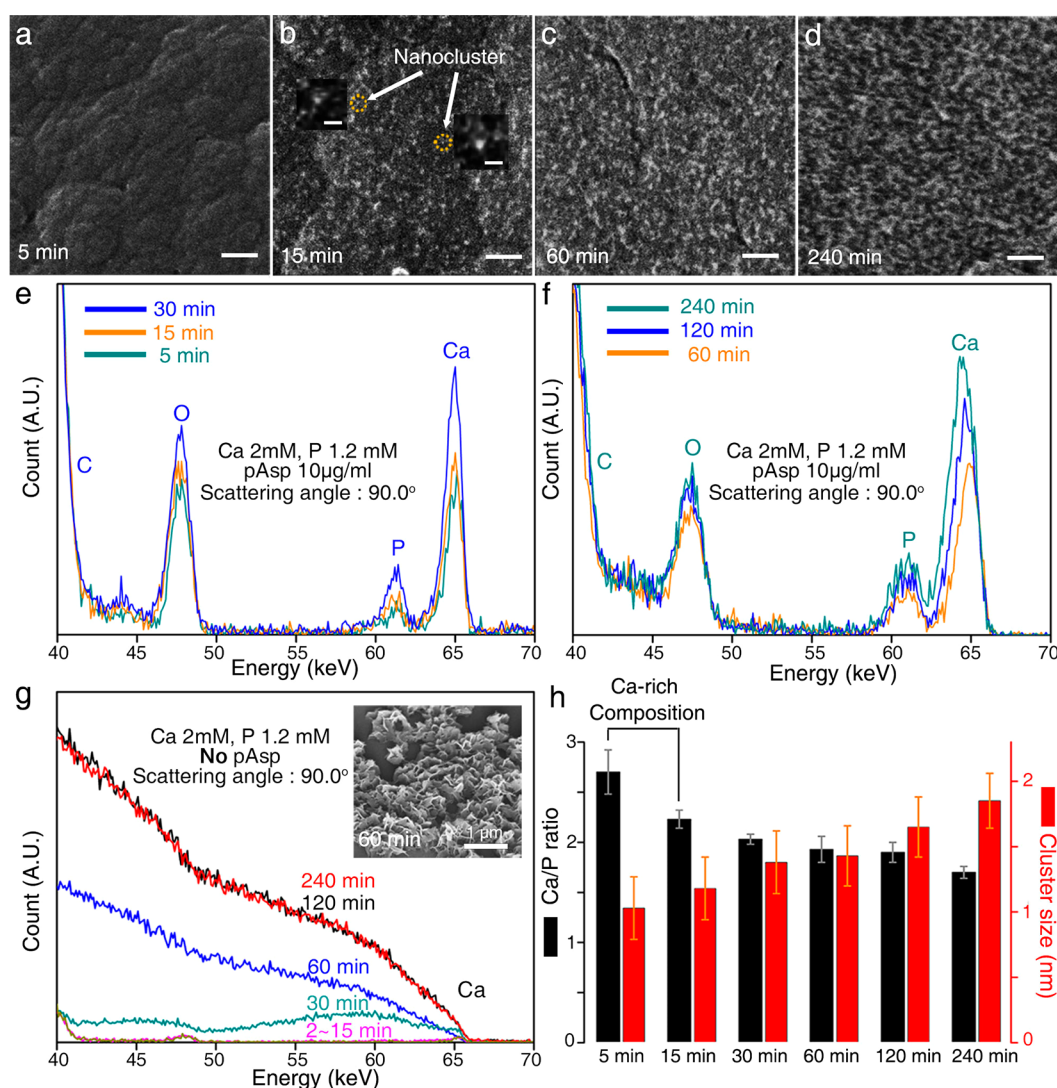


Figure 2. Characterization of the calcium phosphate nanoclusters. (a–d) HIM images of nanoclusters on the DLC substrate in the presence of pAsp (10 µg/mL) with calcium and phosphate ions over time (5, 15, 60, and 240 min) (scale bar: 20 nm). Approximately 1–2 nm clusters were clearly visualized in magnified images of part b (b inset; scale bar, 2 nm). TOF-MEIS spectra of the clusters (e, f) in the presence of pAsp (10 µg/mL) and (g) in the absence of the pAsp. Without pAsp, the calcium and phosphate peaks were merged because of the significantly large size of the clusters. An SEM image of multilayer apatite after 60 min of reaction is displayed in the inset of part g. (h) Calcium-to-phosphate ratio and size of the clusters simulated from the TOF-MEIS spectra in parts e and f.

composed of 2 nm nanoclusters were found with a higher coverage (Figure 2d).

Without pAsp, the formation of calcium phosphate occurred without a controlled manner. Bulky calcium phosphate containing 10–20 nm particles was locally observed by Cs-corrected STEM as shown in Figure 1d. The role of pAsp in stabilizing the initially formed species was also confirmed with AFM, scanning electronic microscopy (SEM), and transmission electron microscopy (TEM) analyses. When pAsp presented within the solution, approximately 1–2 nm in height nanoclusters were found after 30 min of the reaction with AFM (Figure 1f). However, without pAsp, approximately 25 nm thick hydroxyapatite nanoplates had already appeared after 30 min, and the calcifiable substrate was fully covered with these plates after 240 min, as assessed by AFM (Figure 1g,h). TEM results demonstrated that needle-shaped crystalline hydroxyapatite particles were formed after 60 min of reaction in the absence of pAsp, whereas similar crystalline hydroxyapatites were found after 30 days of reaction in the presence of pAsp

(Supporting Information, Figure S2). No other amorphous or crystalline phases were detected by TEM analyses even after 30 days of reaction. These strikingly different growth behaviors depending on the presence of pAsp clearly showed the effect of pAsp on stabilizing the nanocluster and decelerating the growth kinetics.

Quantitative information for the calcium-to-phosphate molar ratio and the size of the observed clusters was directly analyzed with TOF-MEIS measurements. Before the measurements, the samples were rinsed with ethanol and deionized water after calcium phosphate formation to remove the potential TOF-MEIS signals from dried solutes, such as CaCl_2 or KH_2PO_4 , onto the DLC substrates. The rinsed samples were carefully dried with N_2 gas and transferred into the TOF-MEIS chamber. Identical TOF-MEIS signals were found in the samples with various rinsing conditions. The TOF-MEIS spectra of the clusters were recorded at selected times from 5 to 240 min, and their size and compositional ratio were calculated based on the peak width and intensity (Figure

2e,f). As the control, we first monitored the TOF-MEIS spectrum of the calcium phosphate clusters formed in the absence of pAsp (Figure 2g). Because of the burst nucleation and growth, Ca and P MEIS peaks were too broad to identify them separately even at the earliest time point. Eventually, after 60 min of reaction, all peaks involving Ca, P, and O from microscale-thick hydroxyapatite films were completely merged.

In contrast, when pAsp presented inside the reaction solution, Ca and P peaks were clearly observed separately (Figure 2e,f). With their growth, the Ca and P peak intensities and widths increased gradually indicating that the coverage and the size of the clusters increased simultaneously. We first tracked the change in the size of the nanoclusters by simulating the TOF-MEIS spectrum using the Power-MEIS program.¹³ Here, the size of the clusters was calculated on the basis of the peak intensity and width of calcium and phosphorus. The scattering cross-sections of light elements are very low so that pAsp ligands are not included in simulations. Therefore, the cluster sizes calculated from TOF-MEIS spectra were estimated from simulations of individual calcium phosphate spherical cluster size and did not include the size of pAsp. Additionally, the calculated value is the average size of the detected billions of clusters.¹³ After 5 min of the reaction, the average size of the clusters was calculated as ~ 1.0 nm, and their sizes increased up to 1.9 nm after 240 min of the reaction in a stepwise manner (Figure 2h). The calculated size from 1.0 to 1.9 nm was surprisingly consistent with the size of the clusters imaged using Cs-corrected STEM, HIM, and AFM measurements. The change of the Ca, P, and O peak shape is probably due to the size increase and the shape change of calcium phosphate clusters over time.

Interestingly, we found that the relative intensity ratio between Ca and P of the nanoclusters changed over time; particularly, a relatively high Ca-to-P ratio was found in the early stages (Figure 2h). TOF-MEIS simulation showed that 1.0 nm calcium phosphate clusters after 5 min of reaction exhibited a highly calcium-rich composition (Ca/P ~ 2.7) compared to that of the hydroxyapatite (Ca/P ~ 1.67). The ratio gradually approached the value of a hydroxyapatite, arriving at 1.7 after 240 min of the reaction. In detail, the calcium-to-phosphate ratios at the specific sizes were calculated as 2.2 ± 0.1 (size 1.2 ± 0.2 nm), 1.9 ± 0.1 (1.4 ± 0.2 nm), and 1.7 ± 0.1 (1.9 ± 0.2 nm) after 15, 60, and 240 min of the reaction, respectively (Figure 2h). These results were quite interesting as the clusters formed in the absence of pAsp with diverse initial reactant concentration conditions exhibited completely different nucleation and growth behaviors at the same reaction times (Figure 2g and Supporting Information, Figure S3). The uncertainties in the compositional ratio and size were estimated from seven independently prepared samples, carefully simulated using the Power-MEIS program (Supporting Information, Figures S4 and S5 and Table S1).¹³ The uncertainty in the MEIS simulation results generally falls 3% in composition and 0.2 nm in thickness, as reported elsewhere.¹³ Combining TOF-MEIS analysis and the synthetic strategy that inhibits calcium phosphate formation, we could observe the existence of calcium-rich sub-nm clusters and their gradual evolution toward the bulky compositional ratio.

Additionally, we examined the potential influence of the rinsing process on the clusters by varying the times of the rinsing step. We found that overall TOF-MEIS spectra after 15 min of reaction exhibited similar trends, leading to the same results (Supporting Information, Figure S6). Even when we

prepared samples without rinsing, their overall TOF-MEIS spectrum was identical to that of the rinsed sample, except for Cl and S peaks that might originate from dried solutes on the DLC substrates. Moreover, preliminary wet-MEIS systems, which do not require rinsing and dehydration steps, showed the existence of similar calcium-rich clusters with the calcium-to-phosphate ratio of 2.0 after 60 min of reaction (Supporting Information, Figures S7 and S8).

To theoretically understand the unexpectedly calcium-rich compositional ratio in the nanoclusters, we performed first-principles density functional theory (DFT) calculations. First, we modeled the possible structure of the cluster with an experimentally obtained calcium-to-phosphate ratio of 3. Considering its experimental size (~ 0.9 nm), we assumed that the cluster consisted of three Ca^{2+} ions and one phosphate species, where the phosphate species is located in its center (Ca_3P_1 model). Here, in the experimental condition of pH ~ 7.4 , the phosphate species can have one of the three forms of PO_4^{3-} , HPO_4^{2-} , and H_2PO_4^- so that all three types of Ca_3P_1 clusters ($\text{Ca}_3\text{PO}_4^{3+}$, $\text{Ca}_3\text{HPO}_4^{4+}$, and $\text{Ca}_3\text{H}_2\text{PO}_4^{5+}$) were modeled considering their possible combinations (Figure 3a,c,e).

The bare Ca_3P_1 clusters exhibited unstable electronic structures with unpassivated dangling bonds from the DFT analysis (Figure 3b,d,f). On the basis of our experimental observations that pAsp decelerated the growth kinetics, we

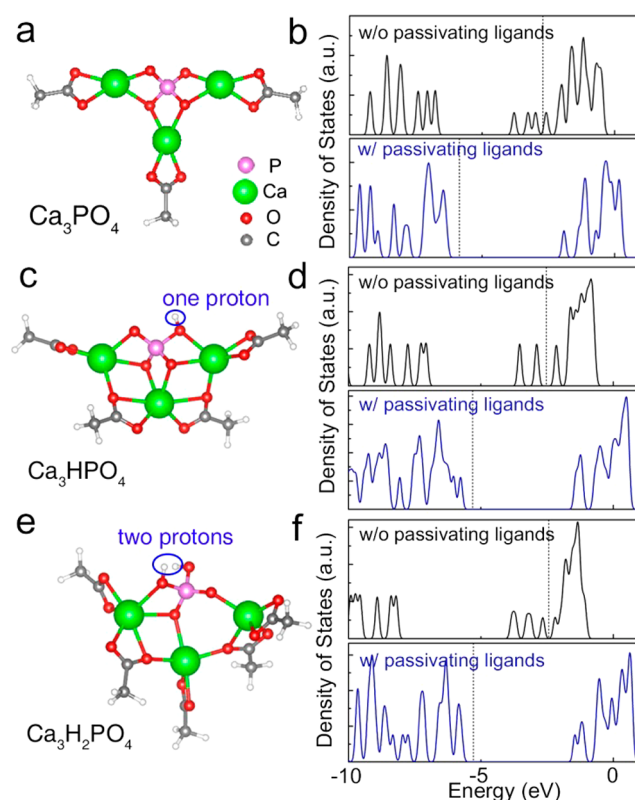


Figure 3. Atomic models of Ca_3P_1 clusters and their stabilization by passivating ligands. (a, c, e) Ball-and-stick models of the Ca_3P_1 clusters and (b, d, f) their electronic structures without (top) and with (bottom) passivating acetate ligands on the surface (a, b, Ca_3PO_4 ; c, d, Ca_3HPO_4 ; and e, f, $\text{Ca}_3\text{H}_2\text{PO}_4$). The Fermi energy is indicated by the dashed lines, and the vacuum level is set to zero. Dangling bond states near the Fermi energy were clearly removed by the ligand passivation.

assumed that negatively charged carboxyl groups in pAsp might stabilize positively charged Ca_3P_1 clusters. Therefore, we employed monomeric acetate groups as simplified structures of pAsp, to our DFT simulations. Interestingly, when we introduced negatively charged acetate groups around the cluster, the bare Ca_3P_1 clusters became very stable by passivating all of the dangling bonds with these negatively charged groups (Figure 3b,d,f). In detail, $\text{Ca}_3\text{PO}_4^{3+}$, $\text{Ca}_3\text{HPO}_4^{4+}$, and $\text{Ca}_3\text{H}_2\text{PO}_4^{5+}$ clusters became stable when three, four, and five negatively charged acetate groups passivated an individual cluster, respectively. Therefore, we propose that an interplay between negatively charged passivating ligands and surface calcium ions led to the thermodynamic stabilization of the exceptionally cation-rich nanoclusters.⁵ As the carboxyl-ligand-passivated Ca_3P_1 pre-clusters were chemically stable with a low chemical potential, the nucleation and growth rate could be significantly reduced by the presence of pAsp. This specific interaction between the ligands and the calcium ions is quite noticeable because the compositional ratio of the clusters formed in the absence of pAsp is significantly different ($\text{Ca}/\text{P} \sim 0.33$), as described in the previous report.²⁹ Although the exact nature of the clusters could be revealed by incorporating diverse ionic species and water molecules in our calculation, we believe that these results might highlight the important role of pAsp on the stabilization of the calcium-rich clusters. Indeed, previous reports represented that a similar calculation method using a vacuum condition could be applied to understand the stabilization process of quantum dots through their interaction with the passivating ligands in the solution.^{36–38}

Additionally, our calculation results showed that the $\text{Ca}_3\text{PO}_4^{3+}$ cluster passivated by acetate groups in pAsp ($\text{Ca}_3\text{PO}_4(\text{CH}_3\text{COO})_3$ model) was very stable compared to that passivated by hydroxyl groups ($\text{Ca}_3\text{PO}_4(\text{OH})_3$ model) (Supporting Information, Figure S9). The formation energy of the acetate-passivated Ca_3PO_4 cluster was approximately -3 eV lower than that of the hydroxyl-passivated counterpart, indicating that hydroxyl groups could not replace the acetate groups that passivate calcium phosphate clusters during rinsing steps. On the basis of rinsing tests and theoretical investigations, we believe that the compositional ratio of the clusters might be negligibly affected by rinsing procedures because of specific interactions between pAsp and calcium-rich clusters.

CONCLUSION

In summary, we investigated the initial stages of heterogeneous calcium phosphate nucleation using the TOF-MEIS technique with sub-nm resolution. We identified nanometer-sized calcium phosphate clusters comprising three Ca^{2+} ions and one phosphate species in a template-guided nucleation and growth process. DFT calculations suggested that the calcium-rich Ca_3P_1 clusters ($\text{Ca}_3\text{PO}_4^{3+}$, $\text{Ca}_3\text{HPO}_4^{4+}$, and $\text{Ca}_3\text{H}_2\text{PO}_4^{5+}$) can be stabilized by a carboxylic passivating template. We believe that our findings utilizing TOF-MEIS can provide a new mechanistic insight for understanding biomineralization and demonstrate the potential of TOF-MEIS for revealing nanoscale cluster chemistry.

METHODS AND MATERIALS

Self-Assembled Monolayer (SAM) Formation. A DLC film with $1\ \mu\text{m}$ thickness on Si substrate was exposed to oxygen

plasma (10 W RF power under 120 mTorr) for 120 s to generate hydroxyl groups on the DLC substrate. Then, the substrate was immersed into 100 mM trimethoxy(7-octen-1-yl)silane (Technical grade 80%, Sigma-Aldrich) dissolved in ethanol overnight. After removal of the unlinked silane residues by washing the substrate with ethanol, carboxylation of the terminal ethylenic double bond in SAM was performed according to previous reports.^{39,40} Briefly, for carboxylation, the substrates were immersed in 5% $\text{KMnO}_4(\text{aq})$ (ACS reagent $\geq 99\%$, Sigma-Aldrich) for 5 min. After formation of the terminal carboxyl group, the substrate was thoroughly washed using deionized (DI) water. For AFM and SEM image analysis, SAM was formed onto the atomically flat Si(111) substrate according to a previous report.⁴¹ In detail, a hydrogen-terminated Si(111) substrate was immersed into 10-methyl undecanoate (99%, Sigma-Aldrich), which is a precursor for monolayer assembly. To make a covalent bond between Si and monomer, the Si substrate was irradiated by UV light (254 nm) for 2 h. After a copious washing with ethanol, the SAM-treated Si was dipped into 250 mM solution of potassium *tert*-butoxide (Reagent grade 98%, Sigma-Aldrich) in dimethyl sulfoxide for 30 s to perform carboxylation.

Calcium Phosphate Clusters Formation. The SAM-treated substrates were incubated in 10 mM of 4-(2-hydroxyethyl)piperazine-1-ethanesulfonic-acid-buffered (HEPES-buffered) mineralization solutions (pH 7.4, 37 °C) containing 2 mM of $\text{CaCl}_2 \cdot 2\text{H}_2\text{O}$ (ACS reagent $\geq 99\%$, Sigma-Aldrich), 1.2 mM of K_2HPO_4 (ACS reagent $\geq 98\%$, Sigma-Aldrich), and 10 $\mu\text{g}/\text{mL}$ of polyaspartic acid (poly(α,β)-DL-aspartic acid sodium salt with a molecular weight of 2000–11 000, Sigma-Aldrich). Before the experiment, either calcium- or phosphate-ion-containing HEPES buffer was kept in a water bath maintained at 37 °C. At the selected times after the calcium source and phosphate source were poured, each substrate was collected from the solution and rapidly rinsed with DI water and ethanol in sequence three times, and then followed by drying with nitrogen gas. In the case of the samples without rinsing steps, the samples were dried with nitrogen gas right after collecting the substrates from the solution. All the substrates were stored in a nitrogen environment before the TOF-MEIS measurement is conducted. For investigating the detailed calcium phosphate formation pathway without pAsp, the above calcium and phosphate solutions were diluted in the absence of pAsp.

Material Characterization. XPS spectra were used to examine the chemical status of the carbon atoms after the SAM treatment. The data were collected with a passing energy of 23.5 eV with a step size of 0.05 eV based on electron spectroscopy (Sigma Probe; Thermo VG Scientific). AFM images of the calcium phosphate clusters onto SAM-treated Si substrates were obtained using XE-100 park systems in noncontact mode. The operating conditions for AFM were 0.4 Hz of the scan rate. The same sample was observed with SEM using an AURIGA setup to compare the microscale morphology of calcium phosphate over the growth time. High-resolution TEM, Cs-corrected STEM analysis, selected area electron diffraction (SAED), and TEM-EDX analyses were performed using an FEI Titan 80–300 microscope operated at 80 keV. For TEM analysis, monolayer graphene supported by lacey carbon grids was incubated in the mineralization solution to obtain a graphical image of cluster growth. HIM analysis was

performed at the Carl Zeiss Microscopy, Ion Microscopy Innovation Center.

Detailed Information Regarding MEIS Spectroscopy.

MEIS has been used to investigate elemental and structural depth profiles of ultrathin nanomaterials, such as gate oxide nanofilms, with single-atomic-depth resolution.^{42,43} Recently, MEIS was applied for the size and the composition measurement of nanometer-sized particles.¹³ MEIS involves elastic scattering and electronic stopping of ions with energies between 60 and 200 keV. Measurements of scattering angle and scattered ion energy determine the mass of target atoms for elemental identification, and the amount of element can be quantified with accurately determined interatomic potentials which are partially screened Coulomb potentials. For 60–200 keV H⁺ or He⁺, the Moliere interatomic potential or the Ziegler–Biersack–Littmark interatomic potential is usually used. One of the main advantages of the MEIS technique is highly quantitative elemental analysis with the well-known scattering cross-sections.¹⁴ Therefore, the typical error in elemental quantitative analysis is less than 5% with typical counting statistics of MEIS. Since the elastic scattering cross-section is roughly proportional to the square of target element atomic number, MEIS is sensitive for high-Z elements and insensitive for low-Z elements. For Ca and P analyzed in this report, the elastic scattering cross-section is low compared to heavy metallic elements. Therefore, the counting statistics in this report is relatively low.

The peak width of MEIS spectra is mainly determined by electronic stopping of ions. The values of electronic stopping power are tabulated as a function of H⁺ and He⁺ projectile energy for many different elements.⁴⁴ For the MEIS spectra simulation in this report, SRIM electronic stopping powers were used based on the Ziegler–Biersack–Littmark equations (SRIM, stopping and range of ions in matter). The electronic stopping powers are measured as the energy loss (eV) per unit number areal density (10¹⁵ atoms/cm²). Additional errors can be added when the areal number density is converted to the thickness of thin films or the nanoparticle size using the bulk number density, as the densities of nanoparticles and ultrathin films are not well-known. Therefore, for the thickness and nanoparticle size determination, the total error can be as large as 10%. Additional errors in MEIS analysis can result from the neutralization efficiency of backscattered primary ions, for conventional MEIS systems with an electrostatic or magnetic energy analyzer. The neutralization efficiency can be measured and corrected.¹⁴ In contrast, the MEIS results in this report are free from the neutralization efficiency error, since we used the TOF technique for energy analysis.¹³

TOF-MEIS Measurements. A TOF-MEIS system was constructed according to a previous report.¹³ TOF-MEIS spectra were obtained at a scattering angle of 90° with an acceptance angle of 3.5° using 80 keV of acceleration voltage. Incident He⁺ ions were rastered over 500 × 750 μm² of DLC substrate with an ion-beam diameter of ~10 μm. The acceptance angle, 3.5°, was chosen to optimize the ion count rate and the energy resolution. For an increase in the signal-to-noise ratio, each sample was analyzed for at least 2 h. The total ion dose density was estimated to be ~2.0 × 10¹⁴ ions/cm², with which the ion-beam damage effect is expected to be insignificant. For one sample, at least three TOF-MEIS spectra were collected to obtain an average spectrum. The TOF-MEIS spectra were simulated using PowerMEIS software with which the sample was fully discretized in space and stored in a large

3D matrix.¹⁵ Each matrix element represents a specific composition, stoichiometry, and material density of the sample in Å scale. In this manner, each cluster could be represented by a specific shape and size. For the following simulations, the Moliere potential was used as the interatomic potential, and the stopping power was calculated using SRIM 2008 software; the straggling was calculated using the Chu model, and the asymmetry parameters were calculated with Casp 5.0 software.^{14,15} With TOF-MEIS, both positive He ions and neutralized He atoms are measured after scattering so that there is no preference for positive or negative ions. For the acquisition of size and composition information on a cluster from the TOF-MEIS measurement, simulated spectra through PowerMEIS were compared with the measured spectrum. If the magnitude of error is in the range of the deviation value of the average size and compositional ratio from the reappearance experiments, the result was considered to be reliable. Tails in the low-energy side of the Ca peak around 65 keV and the P peak around 61 keV might originate from the presence of larger clusters. It should be noted that calcium phosphate clusters were not completely monodisperse as observed in TEM, AFM, and HIM images. The fitness can be estimated by calculating the σ value according to the following equation:

$$\sigma = \sqrt{\frac{\sum_{i=1}^N (\chi_{e,i} - \chi_{s,i})^2}{N}}$$

where $\chi_{e,i}$ and $\chi_{s,i}$ are experimental and simulated MEIS counts in each energy point, respectively, and N is the total number of energy points in the obtained MEIS spectra.

Additionally, to further investigate the possible effect of rinsing steps, we constructed preliminary wet-MEIS systems, which do not require rinsing and dehydration steps. First, monolayer graphene formed onto Cu foils was functionalized with a SAM layer. Then, the SAM-treated monolayer graphene was immersed in calcium phosphate solutions. After reaction, another monolayer-graphene-encapsulated calcium phosphate cluster formed onto the SAM-treated monolayer graphene. After covering another monolayer graphene, supporting substrate [poly(ethylene terephthalate)-based overhead projector (OHP) film] was attached to the monolayer graphene by adhesion polymer [poly(methyl methacrylate), PMMA]. Finally, Cu foils were completely removed with Na₂SO₄, and TOF-MEIS spectra of calcium phosphate nanoclusters intercalated between two graphene layers were recorded.

Simulation Details. First-principles density functional theory (DFT) calculations were performed using Perdew–Burke–Ernzerhof (PBE) exchange–correlation functional implemented in the Vienna *ab initio* simulation package (VASP).^{45,46} A plane-wave basis set and projected-augmented wave (PAW) potentials were used.^{47,48} Atomic forces and electronic energy were relaxed less than 0.02 eV/Å and 10^{−5} eV, respectively. A plane-wave kinetic energy cutoff of 400 eV and a single γ k -point sampling were applied for every supercell. The vacuum layer is approximately 15 Å in cubic supercell. Formation energies of acetate-passivated or hydroxyl-passivated cluster models were calculated using following equation:

$$E_{\text{form}} = E[\text{Ca}_3\text{PO}_4\text{L}_3] - E[\text{Ca}_3\text{PO}_4(\text{OH})_3] - 3E[\text{LH}] + 3E[\text{H}_2\text{O}]$$

where L is OH[−] or CH₃COO[−] ligands.

■ ASSOCIATED CONTENT

Supporting Information

The Supporting Information is available free of charge on the ACS Publications website at DOI: [10.1021/acscentsci.8b00436](https://doi.org/10.1021/acscentsci.8b00436).

Additional data and figures including point EDS spectra, TEM images, SAED patterns, TEM-EDX spectra, TOF-MEIS spectra, wet-MEIS system schematics, and ball-and-stick models (PDF)

■ AUTHOR INFORMATION

Corresponding Authors

*E-mail: nkitae@snu.ac.kr.

*E-mail: dwmooon@dgist.ac.kr.

ORCID

Yong-Hyun Kim: 0000-0003-4255-2068

Ki Tae Nam: 0000-0001-6353-8877

Author Contributions

[†]J.P. and K.D.Y. contributed equally.

Funding

D.M. was supported from the DGIST R&D Program (18-BD-06) of the Ministry of Science, ICT & Future Planning (MSIP). K.D.Y. and K.T.N. were supported by the Global Frontier R&D Program of the Center for Multiscale Energy System funded by the National Research Foundation under the Ministry of Science and ICT, Korea (2012M3A6A7054855), Creative Materials Discovery Program through the National Research Foundation of Korea (NRF) funded by Ministry of Science and ICT (NRF-2017M3D1A1039377), the National Research Foundation of Korea (NRF) grant funded by the Korea government (MSIT) (NRF-2017R1A2B3012003), and the National Research Foundation of Korea (NRF) grant funded by the Korea government (MSIT) (NRF-2018M3C1B7021994). N.-Y.K., V.-D.L., and Y.-H.K. were supported by the National Research Foundation of Korea (2015R1A2A2A05027766), Science Research Center (2016R1A5A1008184), and Global Frontier R&D (2011-0031566) programs of MSIP.

Notes

The authors declare no competing financial interest.

No unexpected or unusually high safety hazards were encountered.

■ ACKNOWLEDGMENTS

D.M. acknowledges technical supports from Doug Wei from Carl Zeiss for HIM imaging.

■ REFERENCES

- (1) Becker, R.; Döring, W. Kinetische Behandlung Der Keimbildung in Übersättigten Dämpfen. *Ann. Phys.* **1935**, *416* (8), 719–752.
- (2) Nielsen, A. E. *Kinetics of Precipitation*; Pergamon: Oxford, 1964.
- (3) Yuk, J. M.; Park, J.; Ercius, P.; Kim, K.; Hellebusch, D. J.; Crommie, M. F.; Lee, J. Y.; Zettl, A.; Alivisatos, A. P. High-Resolution EM of Colloidal Nanocrystal Growth Using Graphene Liquid Cells. *Science (Washington, DC, U. S.)* **2012**, *336* (6077), 61–64.
- (4) Boles, M. A.; Ling, D.; Hyeon, T.; Talapin, D. V. The Surface Science of Nanocrystals. *Nat. Mater.* **2016**, *15*, 141.
- (5) Choi, H.; Ko, J.-H.; Kim, Y.-H.; Jeong, S. Steric-Hindrance-Driven Shape Transition in PbS Quantum Dots: Understanding Size-Dependent Stability. *J. Am. Chem. Soc.* **2013**, *135* (14), 5278–5281.

- (6) Chhowalla, M.; Shin, H. S.; Eda, G.; Li, L.-J.; Loh, K. P.; Zhang, H. The Chemistry of Two-Dimensional Layered Transition Metal Dichalcogenide Nanosheets. *Nat. Chem.* **2013**, *5*, 263.
- (7) Ling, T.; Yan, D. Y.; Jiao, Y.; Wang, H.; Zheng, Y.; Zheng, X.; Mao, J.; Du, X. W.; Hu, Z.; Jaroniec, M.; et al. Engineering Surface Atomic Structure of Single-Crystal Cobalt (II) Oxide Nanorods for Superior Electrocatalysis. *Nat. Commun.* **2016**, *7*, 12876.
- (8) Hong, X.; Liu, J.; Zheng, B.; Huang, X.; Zhang, X.; Tan, C.; Chen, J.; Fan, Z.; Zhang, H. A Universal Method for Preparation of Noble Metal Nanoparticle-Decorated Transition Metal Dichalcogenide Nanobelts. *Adv. Mater.* **2014**, *26* (36), 6250–6254.
- (9) Alvarez, M. M.; Aizenberg, J.; Analoui, M.; Andrews, A. M.; Bisker, G.; Boyden, E. S.; Kamm, R. D.; Karp, J. M.; Mooney, D. J.; Oklu, R.; et al. Emerging Trends in Micro- and Nanoscale Technologies in Medicine: From Basic Discoveries to Translation. *ACS Nano* **2017**, *11* (6), 5195–5214.
- (10) Park, J.; Park, H.; Ercius, P.; Pegoraro, A. F.; Xu, C.; Kim, J. W.; Han, S. H.; Weitz, D. A. Direct Observation of Wet Biological Samples by Graphene Liquid Cell Transmission Electron Microscopy. *Nano Lett.* **2015**, *15* (7), 4737–4744.
- (11) Yuk, J. M.; Zhou, Q.; Chang, J.; Ercius, P.; Alivisatos, A. P.; Zettl, A. Real-Time Observation of Water-Soluble Mineral Precipitation in Aqueous Solution by In Situ High-Resolution Electron Microscopy. *ACS Nano* **2016**, *10* (1), 88–92.
- (12) Snead, M. L.; Zhu, D.; Lei, Y.; White, S. N.; Snead, C. M.; Luo, W.; Paine, M. L. Protein Self-Assembly Creates a Nanoscale Device for Biomineralization. *Mater. Sci. Eng., C* **2006**, *26* (8), 1296–1300.
- (13) Jung, K.-W.; Yu, H.; Min, W. J.; Yu, K.-S.; Sortica, M. A.; Grande, P. L.; Moon, D. Quantitative Compositional Profiling of Conjugated Quantum Dots with Single Atomic Layer Depth Resolution via Time-of-Flight Medium-Energy Ion Scattering Spectroscopy. *Anal. Chem.* **2014**, *86* (2), 1091–1097.
- (14) van der Veen, J. F. Ion Beam Crystallography of Surfaces and Interfaces. *Surf. Sci. Rep.* **1985**, *5* (5), 199–287.
- (15) Sortica, M. A.; Grande, P. L.; Machado, G.; Miotti, L. Characterization of Nanoparticles through Medium-Energy Ion Scattering. *J. Appl. Phys.* **2009**, *106* (11), 114320.
- (16) Hoang, Q. Q.; Sicheri, F.; Howard, A. J.; Yang, D. S. C. Bone Recognition Mechanism of Porcine Osteocalcin from Crystal Structure. *Nature* **2003**, *425*, 977.
- (17) Flade, K.; Lau, C.; Mertig, M.; Pompe, W. Osteocalcin-Controlled Dissolution–Reprecipitation of Calcium Phosphate under Biomimetic Conditions. *Chem. Mater.* **2001**, *13* (10), 3596–3602.
- (18) Glimcher, M. J.; Muir, H. Recent Studies of the Mineral Phase in Bone and Its Possible Linkage to the Organic Matrix by Protein-Bound Phosphate Bonds. *Philos. Trans. R. Soc., B* **1984**, *304* (1121), 479–508.
- (19) Olszta, M. J.; Cheng, X.; Jee, S. S.; Kumar, R.; Kim, Y.-Y.; Kaufman, M. J.; Douglas, E. P.; Gower, L. B. Bone Structure and Formation: A New Perspective. *Mater. Sci. Eng., R* **2007**, *58* (3), 77–116.
- (20) Stetler-Stevenson, W. G.; Veis, A. Type I Collagen Shows a Specific Binding Affinity for Bovine Dentin Phosphophoryn. *Calcif. Tissue Int.* **1986**, *38* (3), 135–141.
- (21) Palmer, L. C.; Newcomb, C. J.; Kaltz, S. R.; Spoerke, E. D.; Stupp, S. I. Biomimetic Systems for Hydroxyapatite Mineralization Inspired By Bone and Enamel. *Chem. Rev.* **2008**, *108* (11), 4754–4783.
- (22) Mahamid, J.; Sharir, A.; Addadi, L.; Weiner, S. Amorphous Calcium Phosphate Is a Major Component of the Forming Fin Bones of Zebrafish: Indications for an Amorphous Precursor Phase. *Proc. Natl. Acad. Sci. U. S. A.* **2008**, *105*, 12748.
- (23) Brečević, L.; Füredi-Milhofer, H. Precipitation of Calcium Phosphates from Electrolyte Solutions. *Calcif. Tissue Res.* **1972**, *10* (1), 82–90.
- (24) Dorozhkin, S. V.; Epple, M. Biological and Medical Significance of Calcium Phosphates. *Angew. Chem., Int. Ed.* **2002**, *41* (17), 3130–3146.

- (25) Posner, A.; Betts, F. Synthetic Amorphous Calcium Phosphate and Its Relation to Bone Mineral Structure. *Acc. Chem. Res.* **1975**, *8*, 273.
- (26) Onuma, K.; Ito, A. Cluster Growth Model for Hydroxyapatite. *Chem. Mater.* **1998**, *10*, 3346.
- (27) Nudelman, F.; Pieterse, K.; George, A.; Bomans, P. H.; Friedrich, H.; Brylka, L. J.; Hilbers, P. A.; de With, G.; Sommerdijk, N. A. The role of collagen in bone apatite formation in the presence of hydroxyapatite nucleation inhibitors. *Nat. Mater.* **2010**, *9*, 1004–1009.
- (28) Dey, A.; Bomans, P. H.; Müller, F. A.; Will, J.; Frederik, P. M.; de With, G.; Sommerdijk, N. A. The role of prenucleation clusters in surface-induced calcium phosphate crystallization. *Nat. Mater.* **2010**, *9*, 1010–1014.
- (29) Habraken, W. J. E. M.; Tao, J.; Brylka, L. J.; Friedrich, H.; Bertineti, L.; Schenk, A. S.; Verch, A.; Dmitrovic, V.; Bomans, P. H. H.; Frederik, P. M.; et al. Ion-Association Complexes Unite Classical and Non-Classical Theories for the Biomimetic Nucleation of Calcium Phosphate. *Nat. Commun.* **2013**, *4*, 1507.
- (30) Gebauer, D.; Kellermeier, M.; Gale, J. D.; Bergström, L.; Cölfen, H. Pre-nucleation clusters as solute precursors in crystallization. *Chem. Soc. Rev.* **2014**, *43*, 2348–2371.
- (31) De Yoreo, J. J. Crystal nucleation: more than one pathway. *Nat. Mater.* **2013**, *12*, 284–285.
- (32) Nielsen, M. H.; Aloni, S.; De Yoreo, J. J. In situ TEM imaging of CaCO₃ nucleation reveals coexistence of direct and indirect pathways. *Science* **2014**, *345*, 1158–1162.
- (33) Hu, Q.; Nielsen, M. H.; Freeman, C. L.; Hamm, L. M.; Tao, J.; Lee, J. R. I.; Han, T. Y. J.; Becker, U.; Harding, J. H.; Dovee, P. M.; et al. The thermodynamics of calcite nucleation at organic interfaces: Classical vs. non-classical pathways. *Faraday Discuss.* **2012**, *159*, 509–523.
- (34) Smeets, P. J.; Cho, K. R.; Kempen, R. G.; Sommerdijk, N. A.; De Yoreo, J. J. Calcium carbonate nucleation driven by ion binding in a biomimetic matrix revealed by in situ electron microscopy. *Nat. Mater.* **2015**, *14*, 394–399.
- (35) Hamm, L. M.; Giuffrè, A. J.; Han, N.; Tao, J.; Wang, D.; De Yoreo, J. J.; Dove, P. M. Reconciling disparate views of template-directed nucleation through measurement of calcite nucleation kinetics and binding energies. *Proc. Natl. Acad. Sci. U. S. A.* **2014**, *111*, 1304–1309.
- (36) Woo, J. Y.; Ko, J.-H.; Song, J. H.; Kim, K.; Choi, H.; Kim, Y.-H.; Lee, D. C.; Jeong, S. Ultrastable PbSe Nanocrystal Quantum Dots via in Situ Formation of Atomically Thin Halide Adlayers on PbSe(100). *J. Am. Chem. Soc.* **2014**, *136* (25), 8883–8886.
- (37) Kim, K.; Yoo, D.; Choi, H.; Tamang, S.; Ko, J. H.; Kim, S.; Kim, Y. H.; Jeong, S. Halide-Amine Co-Passivated Indium Phosphide Colloidal Quantum Dots in Tetrahedral Shape. *Angew. Chem., Int. Ed.* **2016**, *55* (11), 3714–3718.
- (38) Song, H.-W.; Kim, N.-Y.; Park, J.; Ko, J.-H.; Hickey, R. J.; Kim, Y.-H.; Park, S.-J. Shape-Controlled Syntheses of Metal Oxide Nanoparticles by the Introduction of Rare-Earth Metals. *Nanoscale* **2017**, *9* (8), 2732–2738.
- (39) Choi, J.; Ishida, T.; Kato, T.; Fujisawa, S. Self-Assembled Monolayer on Diamond-like Carbon Surface: Formation and Friction Measurements. *Tribol. Int.* **2003**, *36* (4), 285–290.
- (40) Liu, Q.; Ding, J.; Mante, F. K.; Wunder, S. L.; Baran, G. R. The Role of Surface Functional Groups in Calcium Phosphate Nucleation on Titanium Foil: A Self-Assembled Monolayer Technique. *Biomaterials* **2002**, *23* (15), 3103–3111.
- (41) Strother, T.; Cai, W.; Zhao, X.; Hamers, R. J.; Smith, L. M. Synthesis and Characterization of DNA-Modified Silicon (111) Surfaces. *J. Am. Chem. Soc.* **2000**, *122* (6), 1205–1209.
- (42) Gusev, E. P.; Copel, M.; Cartier, E.; Baumvol, I. J. R.; Krug, C.; Gribelyuk, M. A. High-Resolution Depth Profiling in Ultrathin Al₂O₃ Films on Si. *Appl. Phys. Lett.* **2000**, *76* (2), 176–178.
- (43) Kim, Y. P.; Choi, S. K.; Kim, H. K.; Moon, D. W. Direct Observation of Si Lattice Strain and Its Distribution in the Si(001)–SiO₂ Interface Transition Layer. *Appl. Phys. Lett.* **1997**, *71* (24), 3504–3506.
- (44) Andersen, H. H.; Ziegler, J. F. *Hydrogen. Stopping powers and ranges in all elements. [10 keV to 20 MeV (per amu)]*; Pergamon Press: New York, 1977.
- (45) Perdew, J. P.; Burke, K.; Ernzerhof, M. Generalized Gradient Approximation Made Simple. *Phys. Rev. Lett.* **1996**, *77* (18), 3865–3868.
- (46) Kresse, G.; Furthmüller, J. Efficient Iterative Schemes for Ab Initio Total-Energy Calculations Using a Plane-Wave Basis Set. *Phys. Rev. B: Condens. Matter Mater. Phys.* **1996**, *54* (16), 11169–11186.
- (47) Kresse, G.; Joubert, D. From ultrasoft pseudopotentials to the projector augmented-wave method. *Phys. Rev. B: Condens. Matter Mater. Phys.* **1999**, *59* (3), 1758–1775.
- (48) Blöchl, P. E. Projector augmented-wave method. *Phys. Rev. B: Condens. Matter Mater. Phys.* **1994**, *50* (24), 17953–17979.